J Mater Sci (2012) 47:6801–6811
DOI 10.1007/s10853-012-6624-7

Reinforcement of Ag nanoparticle paste with nanowires for low temperature pressureless bonding

Peng Peng · Anming Hu · Boxin Zhao · Adrian P. Gerlich · Y. Norman Zhou

Received: 13 February 2012 / Accepted: 28 May 2012 / Published online: 9 June 2012

Abstract Low temperature interconnection processes for lead-free packaging and flexible electronics are currently of great interest. Several studies have focused on bonding using silver nanoparticles (Ag NPs) or copper nanoparticles (Cu NPs). However, pressure assistance is generally necessary for bonding with nanomaterial pastes, which limits its industrial applications. Here, a unique method for bonding of copper wires using Ag NP and nanowire binary pastes is examined, in which joining is accomplished from 60 to 200 °C and yet without the application of pressure. Bonding is facilitated by solid state sintering of Ag nanomaterials and metallic bonding between Cu and Ag interfaces. The effects of different additions of Ag nanowires in bonded joints are studied, in which addition of 20 vol% Ag nanowires improves bonding strength after low temperature sintering by 50–80 % compared with Ag nanoparticle paste. A mechanical reinforcement effect due to introduction of Ag nanowires has been confirmed by observation of the fracture path propagation, where necking, breakage and pullout of nanowires occur on loading. This low temperature pressureless bonding technology has the potential for wide use for interconnection in lead-free microcircuits and flexible electronic packaging.

P. Peng (✉) · A. Hu · A. P. Gerlich · Y. N. Zhou
Centre for Advanced Materials Joining,
Department of Mechanical and Mechatronics Engineering,
University of Waterloo, 200 University Avenue West,
Waterloo, ON N2L 3G1, Canada
e-mail: p5peng@uwaterloo.ca

P. Peng · B. Zhao · Y. N. Zhou
Waterloo Institute for Nanotechnology, University of Waterloo,
200 University Avenue West, Waterloo, ON N2L 3G1, Canada

B. Zhao
Department of Chemical Engineering, University of Waterloo,
200 University Avenue West, Waterloo, ON N2L 3G1, Canada

Introduction

The use of lead alloy solder materials in the electronics industry has raised much concern due to health, environmental and safety issues worldwide [1–6]. With the development of nanotechnology, environmentally friendly and flexible electronic products are becoming more feasible in the near term [7–11]. The use of metallic nanoparticles (NPs) combined with ink-jet printing processing for flexible electronics manufacturing, is a well-known technique in which the deposition and patterning are simultaneously accomplished by printing a solution of the active materials (e.g. Metallic NPs or conductive polymers), and has been widely studied [12–16]. The material deposited using an ink-jet typically consists of gold or silver NPs encapsulated within protective shells and dispersed in a liquid solvent [17, 18]. Recently, nanoscale diffusion bonding using metallic nanomaterials has displayed significant advantages over conventional soldering or adhesive bonding, such as lower bonding temperatures and higher diffusion rate [19]. Hence, low temperature interconnection processes using metallic NP paste appears to be a promising alternative for Pb-free electronic packaging and flexible electronic interconnections [20, 21]. For example, several studies have focused on low temperature joining technology for lead-free packaging or power modules using NPs made from silver [22, 23], copper [24] and gold [25], respectively. The sintering of silver NPs and their bonding to copper wires and substrates to form a 3-D bonded network which can withstand higher working temperatures through further sintering has been reported by

Hu et al. [20] and Alarifi et al. [26]. The typical sintering temperature ranges from 150 to 300 °C are lower than the melting point of the corresponding bulk materials, due to the size effect of NPs [27]. However, pressure is required to facilitate the bonding processing in these studies, which is still inconvenient for industrial applications.

Recently, there is increasing interest in applications of 1-D micro-sized/nano-sized materials, for example, developing multifunctional composite materials incorporating second phase fibres and/or whiskers [28–36]. In carbon materials, mullite fibres were added, which bend and fracture to several fragments that could partially carry the applied loading [37]. For a solder material, Coughlin et al. [38] reported that Ni–Ti shape memory alloy fibres embedded into a Sn-rich solder alloy could improve fatigue and mechanical shock properties of the materials by a super-elasticity transformation property of the fibres on loading. Ongoing efforts are being made to study the sintering of nanowires, nanorods and nanobelts, in order to further exploit the unique properties of these materials [39–43]. However, few have examined the behaviour of metallic joints when nanowires are introduced as a second phase in the bonding material.

This study focuses on a low temperature pressureless bonding process for robust wire to wire bonding of copper by introducing silver nanowires (Ag NW) into a silver nanoparticle (Ag NP) paste in a novel joining material. The bonds were formed by solid state sintering of Ag nanomaterials and metallic bonding between Cu and Ag interfaces. The mechanisms of reinforcement by addition of Ag NWs in joints are discussed in this paper. Ag NPs and Ag NWs sintered at low temperature without pressure can form 3-D networks which provide enhanced strength and fracture resistance of the joint. This methodology provides a novel possibility for bonding and interconnection in the microelectronics industry using Ag nanopastes.

Experiments

All the chemicals and reagents were of analytical grade and used in the as received form without any purification. The synthesis of the Ag NP material involved reacting silver nitrate ($AgNO_3$, Alfa Aesar) and sodium citrate ($C_6H_5O_7Na_3{\cdot}2H_2O$, Alfa Aesar) at 80–90 °C [26]. Ag NWs were prepared in a polyol solution using a method modified from the literature [44, 45]. In this study, 330 mg polyvinylpyrrolidone or PVP ($(C_6H_9NO)_n$, K25, $M_W = 24000$, Alfa Aesar) and 12.5 mg silver chloride (AgCl, Alfa Aesar) were mixed with 40 mL ethylene glycol (EG, Fisher Chemical) in a round-bottom flask. The mixture was heated to between 160 and 170 °C. Then, 110 mg silver nitrate was dissolved in 10 mL ethylene glycol liquid and added into the mixed solution while stirring vigorously and continuing the reaction conditions for 4 h. The Ag NPs and Ag NWs were condensed by centrifugation at 4000 rpm using a 50 mL centrifuge pipe. The clean supernatants were removed from the centrifuge pipes using a pipette resulting in highly concentrated Ag NP and Ag NW pastes. The excess PVPs in Ag NWs could be washed and removed by deionized (DI) water and repeated centrifugation. 0, 10, 20 and 30 % volume fractions of Ag NW paste were mixed with Ag NP paste in 20 mL glass vials by stirring and are designated as Ag NP, Ag NP/10NW, Ag NP/20NW and Ag NP/30NW, respectively.

The copper wires (99.9 % purity) used in this study, from Arcor Electronics, Northbrook, IL, were 250 μm in diameter. Before bonding, the wires were cut into 60 mm pieces and ultrasonically cleaned in acetone for 3 min to remove the organics, 1 % diluted $AgNO_3$ for 1 min to remove the oxide layer and rinsed in ultrapure water (electrical resistivity approximately 18 MΩ cm). A fine needle attached on a 10 mL syringe was used to locate the Ag nanopaste between two clean copper wires on a 60 °C hotplate surface. After depositing 0.05 mL Ag nanopaste, the assembly of copper wires and paste was heated at 60–200 °C in air for 1 h without bonding pressure.

Tensile shear testing was conducted by loading the wires in the axial direction at a rate of 0.5 mm/min using a micro tensile tester (Instron 5548, UK). The cross-sections of bonded samples were mounted using epoxy resin and polished with 1 μm Al_2O_3 powder. Optical microscopy (Olympus BX 51M, Japan) and field-emission scanning electron microscope (Leo 1530 FE-SEM; Zeiss, Germany) were used to study the microstructure of cross-sections, interfaces and fracture surfaces of bonded samples. Energy-dispersive X-ray spectroscopy (EDX, EDAX Pegasus 1200) was employed for elemental analysis. The sintered Ag NPs and Ag NP/NW were also observed using SEM.

Results and discussion

Microstructures of sintered Ag NPs and Ag NWs

Figure 1 shows the microstructures of Ag NP and Ag NW pastes after centrifuging. Figure 1a, b are low magnification SEM images of as-centrifuged Ag NP and Ag NW pastes. The Ag NPs were 50–100 nm in size, with polyhedron morphology as shown in Fig. 1c. The Ag NWs had a pentagonal shape as shown in Fig. 1d with lengths of 8–15 μm and 50–100 nm in thickness. Few Ag NPs were also observed in the Ag NW paste synthesised by the polyol method.

The Ag NP/NW pastes were sintered at different temperatures to investigate the sintering behaviours of these

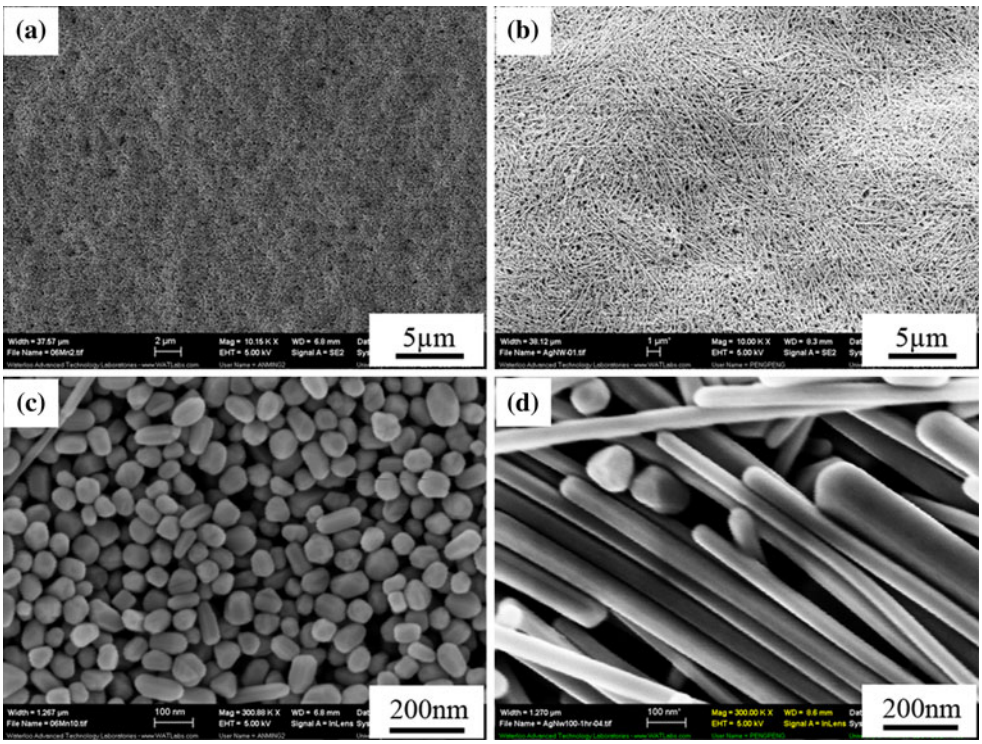

Fig. 1 Microstructure of condensed **a** Ag NP and **b** Ag NW paste after centrifuging. High magnification SEM images of **c** polyhedron-shaped Ag NPs and **d** pentagon-shaped Ag NWs with length of 10–20 μm and 50–100 nm thickness

mixtures at low temperature as shown in Fig. 2. For comparison, unsintered Ag NP/20NW binary paste is shown in Fig. 2a. The microstructures of Ag NP/20NW binary pastes sintered at 60, 100, 150 and 200 °C for 1 h, respectively, are shown in Fig. 2b–e. The average width of bridge paths between adjacent Ag NP–NP and Ag NP–NW grew from 26 ± 2 to 54 ± 4 nm (average of five measured values) as temperature increasing from 60 to 200 °C as indicated by the arrows in Fig. 2b, e; which is consistent with the increased rate of solid-state diffusion and growth of bridge paths expected when the temperature increases. It is worth mentioning that residual PVP from the synthesis process of the Ag NWs, and amorphous citrate complexes from the synthesis process of Ag NPs could be present at the interfaces of the particles and influence the sintering of the paste. Although PVP does not readily decompose at below 300 °C [46, 47], the majority of this material would be removed during the process of washing with DI water as previously shown when the PVP coating was washed from Cu NPs [24]. As such, it would be expected that the particle surface free of PVP is active for low temperature sintering. The amorphous citrate complexes on the surfaces of the Ag NPs will readily vaporise and decompose (at temperatures above 90 °C) and should completely disappear during low temperature sintering [20, 48, 49]. This accounts for the rapid formation and growth of bridges even at temperatures of 100–150 °C. Sintered Ag NP/NW mixed pastes with various additions of Ag NWs at 150 °C are also shown in Fig. 2f, g, i, corresponding to 0, 10 and 30 % Ag NWs by volume in the pastes (20 % is shown in Fig. 2d). Based on the dispersion of the Ag NWs, it is clear they did not aggregate together and were uniformly dispersed in the Ag NP paste by stirring. The inset images of Fig. 2g, i illustrate the morphology of 10 and 30 % Ag NW at a low magnification. Introducing a large fraction of Ag NWs can change the packing of the nanomaterials in joints since spherical particles can be packed more densely than long wires. This leads to the presence of a higher degree of porosity in the sintered 30 % NW paste as shown in the inset Fig. 2j, compared with the paste-containing 10 % Ag NW(see Fig. 2h).

Joining behaviour of Ag NP paste with NW

Figure 3 illustrates the schematic diagram of the tensile shear test samples used to investigate the mechanical performance of the bonded samples. After clamping each bonded sample into the grips as shown in Fig. 3, loading was applied. The measured strength of joints is the tensile shear strength due to the applied shear stress during the tensile testing, because two Cu wires were not coaxial. It was estimated by dividing the highest failure force value by the bonding area [24, 50, 51], $\sigma = F_{\max}/A$ (N/mm^2 or MPa). The fracture area of samples was difficult to measure

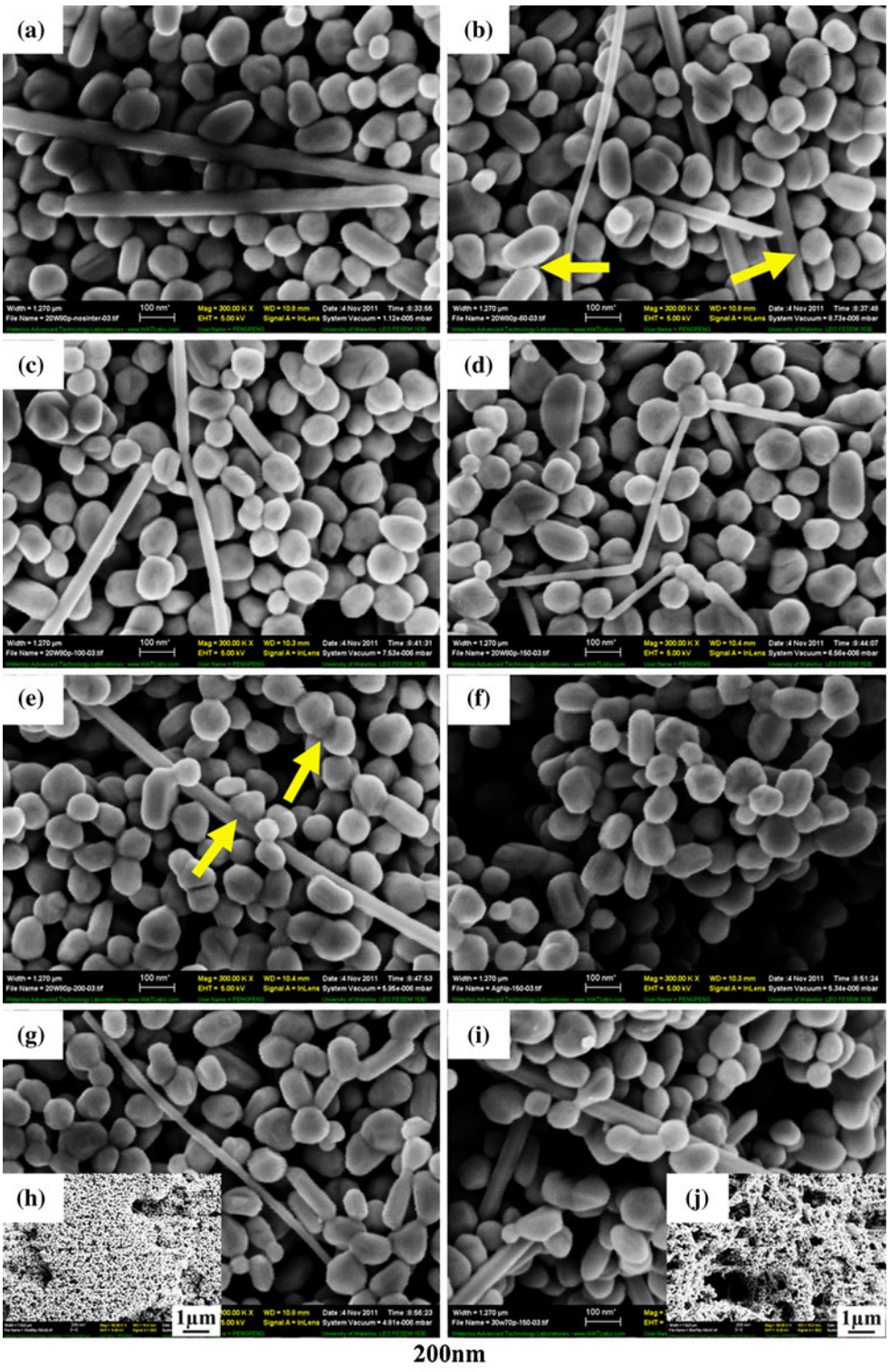

Fig. 2 SEM images of Ag NP/NW paste sintered at different temperatures: **a** unsintered Ag NP/20NW paste, and sintered Ag NP/20NW paste at **b** 60 °C, **c** 100 °C, **d** 150 °C and **e** 200 °C for 1 h with *arrows* highlighting the bridge paths between NP–NP and NP–NW. Sintered paste with different Ag NW volume additions **f** 0 vol%, **g** 10 vol% and **i** 30 vol% after sintering at 150 °C for 1 h. *Inset* low magnification image **h** and **j** are corresponding to Ag NP/10NW and Ag NP/30NW pastes

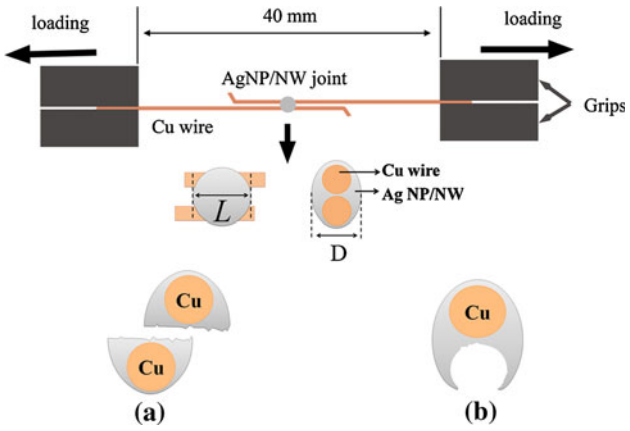

Fig. 3 Schematic illustration of tensile shear strength testing of bonded samples. The starting distance between the grips was fixed at 40 mm, *L* and *D* denote the bonding length and thickness of joint. During testing, two fracture modes for various NW contents: **a** filler material fracture and **b** interfacial fracture on the Cu wire and Ag nanopaste joint interface

due to the unsymmetrical geometry of fracture region. Here, we used average bonding area to normalize the actual fracture area, which bonding area *A* was calculated by multiplying the maximum bonding length *L* by thickness *D* of the Ag-bonding material. Two predominant fracture modes were observed during testing, one being filler material fracture (failure of the sintered Ag NP/NW) as shown in Fig. 3a, and the other was interfacial fracture at the Cu–Ag interface with one wire being pulled-out of the sintered Ag bond material under loading, as shown in Fig. 3b. The fracture modes of all test samples bonded at different temperatures are summarized in Table 1. Filler material fracture was usually observed when 0 and 30 % Ag NW was introduced. The samples tested using Ag NP paste with 10 or 20 % NW all involved failure by interfacial debonding. In addition to these failure modes, fracture of the Cu wire occurred in the sample bonded using Ag NP/20NW paste which was sintered at 200 °C.

The strength of bonded samples as a function of Ag NW volume fraction in the silver paste at different bonding temperatures is presented in Fig. 4a. The remarkable improvement in joint tensile shear strength is suggested to

Table 1 The fracture modes for bonded joints with various Ag NW contents at different temperatures

Temperature (°C)	Ag NP	Ag NP/10NW	Ag NP/20NW	Ag NP/30NW
60	F	I	I	F
100	F, I	I	I	F, I
150	F	I	I	F
200	F, I	I	I, W	F

F, *I* and *W* denote the filler material fracture, interfacial fracture and wire fracture

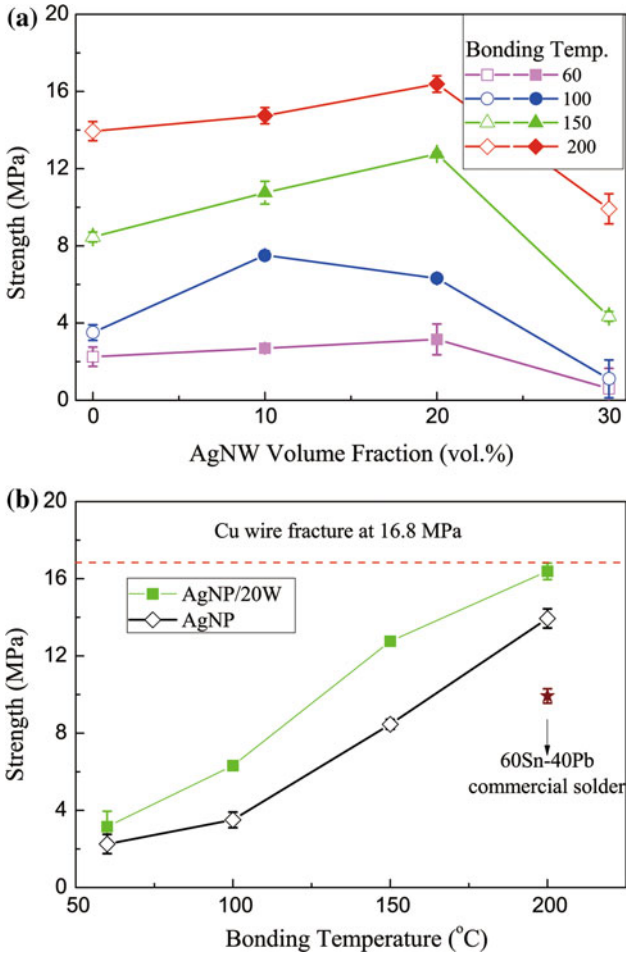

Fig. 4 **a** Bond strength of bonded samples as a function of Ag NW volume fraction at different bonding temperatures. *Squares*, *circles*, *triangles* and *diamonds* represent tested samples bonded at 60, 100, 150 and 200 °C, respectively. *Open* and *closed symbols*, representing the filler material fracture and interfacial fracture, indicate the dominated fracture mode of bonded samples with various Ag NW contents. The *dashed line* denotes the fracture strength of copper wires. **b** The bond strength of bonded samples of Ag NP/20NW and Ag NP pastes as a function of bonding temperature. *Star* represents 60Tin/40 % lead commercial solder joint soldered at 200 °C

be the result of reinforcement provided by the Ag NWs when 100 and 150 °C sintering temperatures are used. The addition of 10 or 20 % volume fraction of Ag NW to the Ag NP paste increased the joint strength by 18–81 % when the same sintering temperatures are applied. However, the strength decreased considerably when 30 % Ag NWs were used due to the porous structure produced in the joint, as shown in Fig. 2j. The highest strength increase was obtained using 20 % Ag NWs by volume, providing an improvement of 50–80 % after sintering at 60 and 100 °C bonding temperatures. Figure 4b shows the strength of bonded joints with Ag NP/20NW binary pastes and Ag NP paste as a function of bonding temperature. The presence of 20 % NW in the bonded joints clearly increased the

failure strength compared to those without Ag NW addition at all bonding temperatures investigated. For comparison, the Cu wires were also joined by soldering (using commercial 60Sn–40Pb solder) at 200 °C, and this joint achieved a strength of 9.9 ± 0.4 MPa compared to 16.4 ± 0.4 and 13.9 ± 0.5 MPa achieved using Ag NP/20NW binary pastes and Ag NP paste, respectively. Prior studies investigating bonding with other paste materials have also reported lower strengths when using Cu NPs (10 MPa) [24] or Ag NPs (8 MPa) applied with 5 MPa pressure [20]. A mean tensile shear strength of 3.2 ± 0.8 MPa was obtained near room-temperature (60 °C) using Ag NP/20NW binary pastes. The incorporation of 10 to 20 % Ag NWs improved the strength of joints and shifted the failure area to the Cu–Ag interface instead of within the sintered silver, due to the reinforcement of the sintered material by the nanowires.

To investigate the fracture mechanism of the sintered Ag NP/NW material, the fracture surfaces were examined by SEM. Figure 5a–d shows the SEM images of the secondary cracks produced perpendicular to the fracture surfaces in joints bonded at 150 °C with Ag NW volume fractions from 0 to 30 %. The regions reveal the role of the NW in the fracture of the bonding material, since the primary crack can not be readily characterized after failure. With the volume fraction of Ag NWs increasing from 10 to 30 %, progressively more crack bridging by the nanowires occurs. Crack propagation is suppressed by bridging of the nanowires, in a similar way to fibre-reinforced composites [49]. Since each Ag NW was bonded with several Ag NPs, this reduced the tendency for pull-out of the NW. Clear evidence of plastic deformation of individual Ag NW was observed as shown in Fig. 5c. The fractured joints with 30 % Ag NW addition exhibited a much lower density of particles than those with 10–20 % Ag NW addition, due to the highly porous sintered structure discussed earlier (see Fig. 2h, j). The accounts for the dramatically decreased bond strength when a 30 % Ag NW volume fraction was used (see Fig. 4a), which also hampered the sintering process at lower temperatures. Moreover, the weaker bond strength between Cu wire and Ag NW compared to Cu and Ag NP is likely attributed to the lower interfacial bonded area resulting from the high porosity.

The cross-sections of fractured joints bonded with Ag NP/20NW paste are shown in Fig. 6. Figure 6a–c is taken by optical microscopy while Fig. 6d–f is SEM images of the bonded interface. In Fig. 6a, pull-out of the Cu wire is clearly identified by the dashed circle indicating the original location of the second Cu wire. Some residual Ag can be observed on the surface of the Cu wire after testing as indicated in Fig. 6b. The bond interface of Cu–Ag is

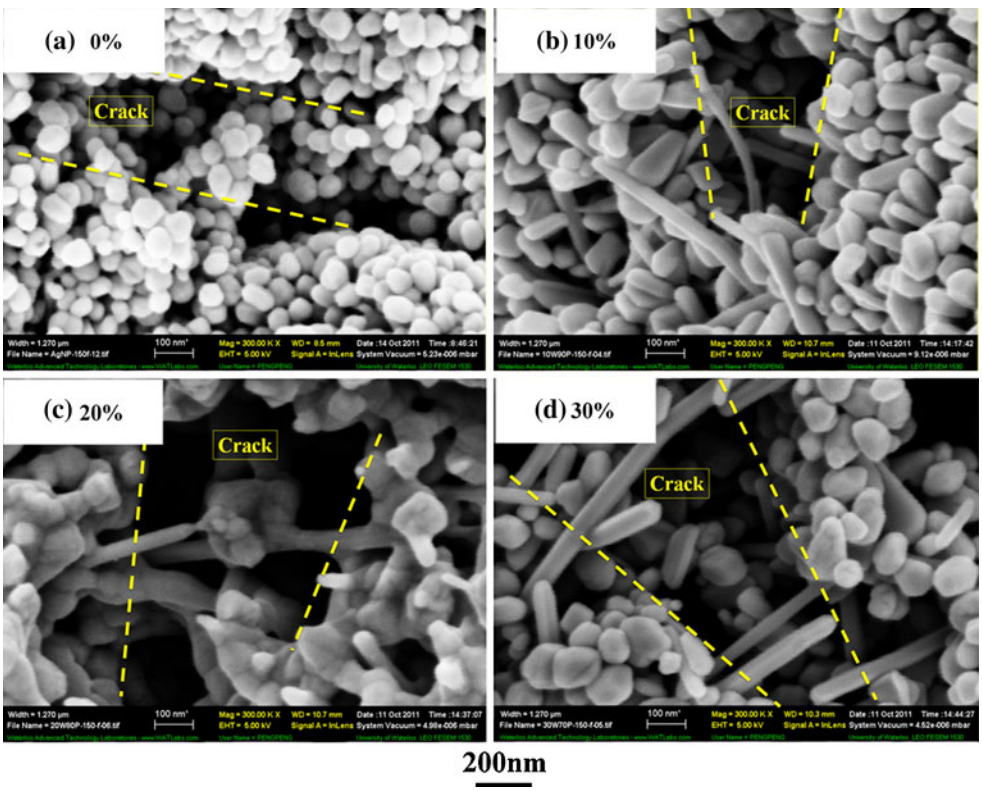

Fig. 5 Microstructure of fracture Ag surface of NW reinforced Ag NP joints bonded at 150 °C with various Ag NW contents from **a** 0 vol%, **b** 10 vol%, **c** 20 vol%, **d** 30 vol%. Cracks are indicated by *dashed lines*

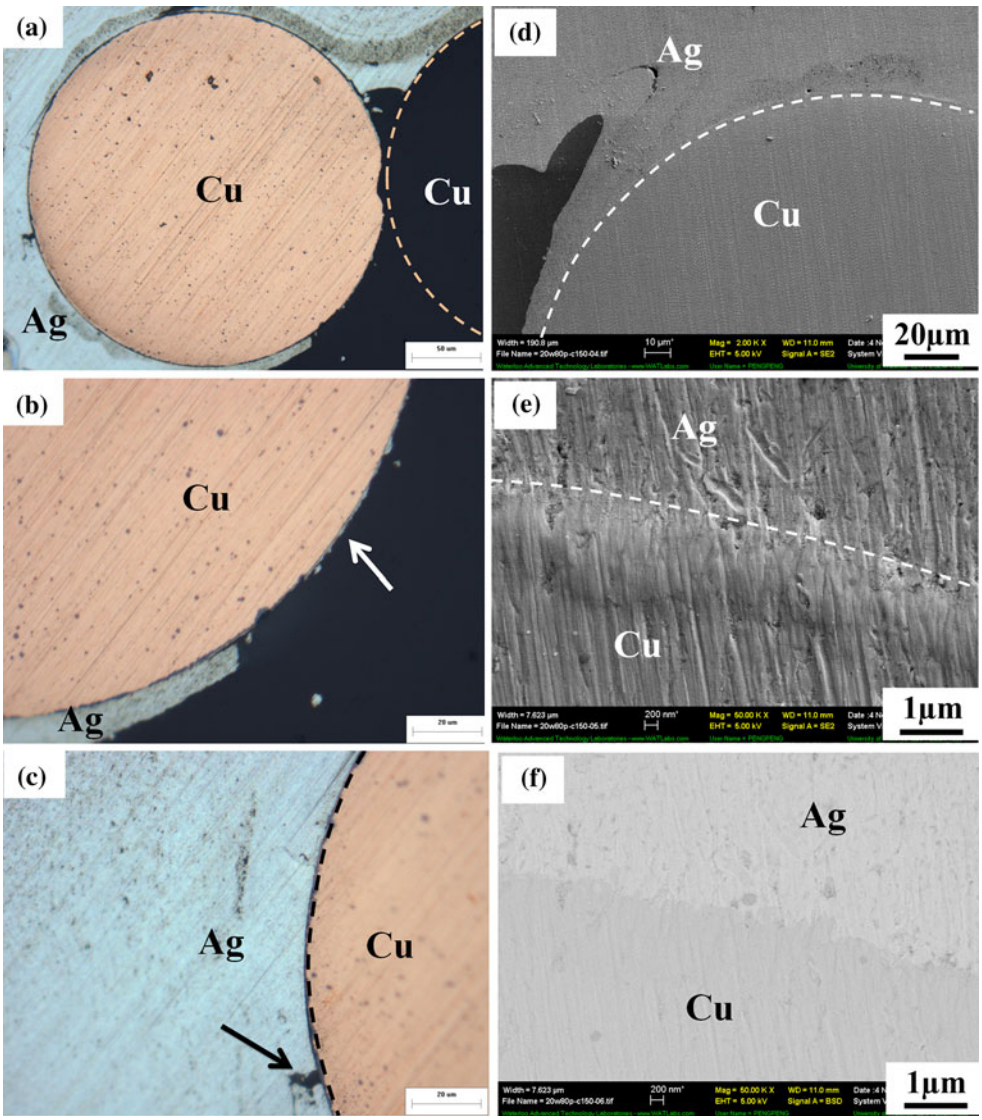

Fig. 6 Microstructures of cross-sections of Ag NP/20NW paste bonded Cu–Cu joints: the pulled-out Cu wire can be identified by *dashed line* in an optical microscope image (**a**). **b** Ag matrix attached on the surface of bare Cu wire and **c** bonded interface of Cu–Ag with pore highlighted by *arrow*. *Right column* **d** SEM image of bonded interface of cross section. **e** High magnification of interface shows lack of gap or debonding area between the Ag-sintered nanomaterials and Cu wire. **f** The backscattered electronic SEM image for the interface, *dark area* denoting the Cu and *bright area* for Ag

clearly shown in Fig. 6c and the pores observed may be due to a locally unbonded area resulting from air bubbles introduced in the paste during bonding or an oxide layer on the Cu surface. A joint cross-section free of microporosity using Ag NP/20NW binary pastes was observed, see Fig. 6d, similar to the pressure bonded joints using Ag NPs [26, 52]. However, the presence of nanopores is general in the joint with low temperature pressureless bonding. In the interface as shown in Fig. 6e, the metallurgical bond between the Cu wire and the Ag paste was found to be continuous. The backscattered electron SEM image Fig. 6f indicates continuity along the Cu/Ag interface. A region below the dashed line with 1 μm in thickness which is actually raised from the surface considering the scratches on the surface formed during the polishing process. This surface relief is common in metallographic samples where a phase is slightly harder, such as an intermetallic compounded, and is not removed as much as the softer Ag or Cu. It is believed that the interdiffusion of Ag and Cu atoms occur along the interface formed a mixed region or interphase boundary layer at the interface [53, 54].

To further study the Cu–Ag interface characteristics, the fractured joints bonded with Ag NP/20NW binary pastes were investigated by SEM and EDX. Figure 7a was taken from the fractured interface on Ag filler material side (as schematic illustrated in Fig. 3b) and Fig. 7b was from the

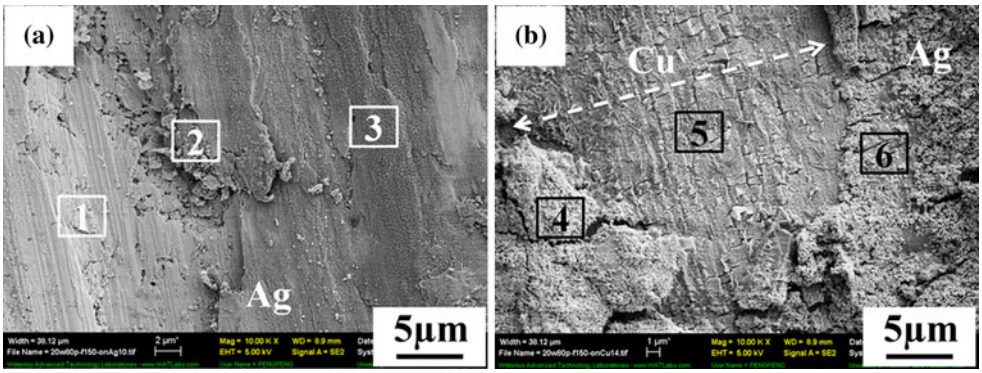

Fig. 7 SEM images of Cu–Ag interface: **a** Ag NP/20NW paste side with labelled *1–3* three points of interest. **b** Cu wire side with *4–6* points of interest, *dotted line with arrows* indicating the Cu wire

surface of pulled-out Cu wire with residual Ag NPs and Ag NWs. Three different spots with different microstructures on both sides were studied using EDX. The results shown in Table 2 indicated that Cu and Ag elements existed on both sides, which supports the notion that interdiffusion occurred and metallic bonding is present at the Ag and Cu interface during low temperature pressureless sintering, similar to previous findings [20].

Table 2 EDX results of selected points on two different sides of the interface of a joint bonded with Ag NP/20NW paste at 150 °C

Interface	Numbers	O (At%)	Cu (At%)	Ag (At%)
Ag side	1	11	6	83
	2	–	34	66
	3	15	66	19
Cu side	4	–	7	93
	5	–	98	2
	6	–	78	22

Fracture behaviours of bonded joints

The load–displacement curves of bonded samples using Ag NP and Ag NP/NW also reveal some key aspects which control the bonding strength. Typically, the load–displacement curves of the joints produced using Ag NP/10NW paste developed a stepwise profile, and were distinct from that of Ag NP paste bonded joints even though similar maximum failure forces are produced, see Fig. 8. It is speculated that the stepwise failure is due to the integrative effects of debonding on Ag NP–NP, NW–NP and NW–NW interfaces, and breaking of the Ag NWs. The quality of the joints can also be evaluated by comparing the bonding energy per unit area or fracture energy [53], i.e. the integrated area under the force–displacement curve shown in Fig. 8 divided by bonding area (the unit is thus in J/m^2 or N/m). It was found that the fracture energy of the Ag NP/10NW bonded at 60 °C was about three times larger than that of the Ag NP joint, although they had similar maximum failure load and bonding area. A larger integrated area requires more energy dissipation during fracture and thus yields higher quality of joints which are more damage tolerant [55, 56].

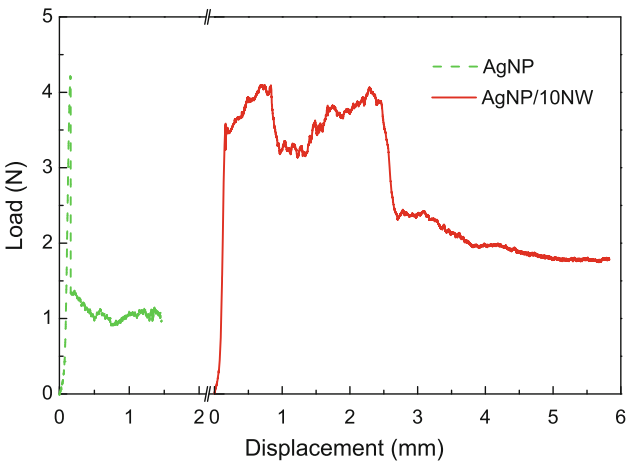

Fig. 8 Typical load–displacement curves of bonded joints: *solid line* for Ag NP/10NW and *dashed line* for Ag NP

To study the behaviour of Ag NWs in joints bonded with Ag NP/NW pastes, the fracture surfaces of tested joints were characterized by SEM. Four different morphologies of Ag NWs were identified on the fracture surfaces and crack areas in Fig. 9. The Ag NWs can be bent (Fig. 9a) and pulled-out (Fig. 9b). In Fig. 9b, some residual NPs highlighted by arrows attached to the end of a pulled-out Ag NW indicate that the debonding of Ag NP–NW actually occurs within the paste matrix. This demonstrates that the Ag NP and Ag NW bonding strength is relatively weak. Morphological features found on the fracture surface included necking of the Ag NWs as highlighted by the arrows in Fig. 9c and even breaking as shown in the circles

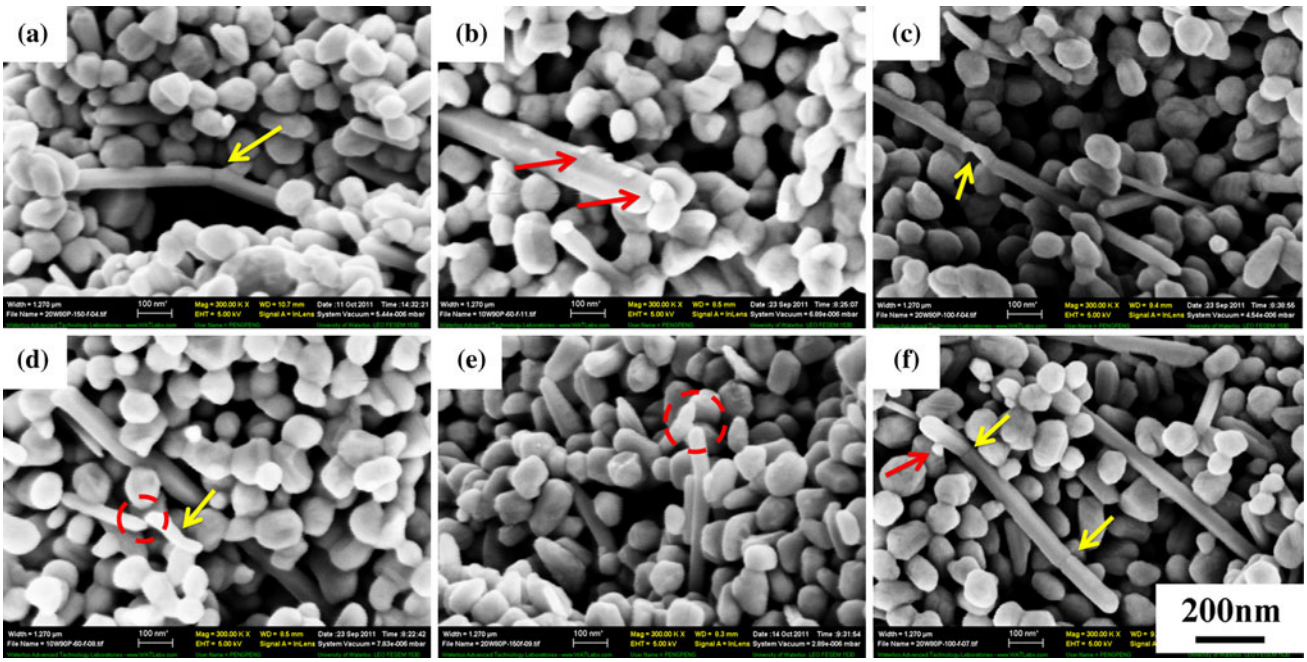

Fig. 9 SEM images of silver nanowires in joints after testing: **a** NW bent under stress with *arrow* indicating the bend region. **b** NW pullout, *arrows* highlighting residual NPs attached on the top and wall of NW. **c** Plastic deformation of NW with deformation regions highlighted by *arrows*. **d** NWs broken under stress, deformation region in the NW is shown. Not individually, the combined actions of Ag NWs are illustrated: **e** Bent NW was broken into two wires under stress, the fracture areas stayed in the *circle*. **f** NW was bent and pulled-out, plastic deformation zones are highlighted by *arrows*. *Dashed lines* indicate the cracks

of Fig. 9d. These phenomena are all likely to occur simultaneously due to the wide range of stress distributions in the NW which are randomly oriented. In Fig. 9e a pair of bent and fractured Ag NW fragments is evident, and even bending and plastic deformation zones in a NW are observed in Fig. 9f, with the necked regions highlighted by arrows. Due to the nano-scale effects, one would expect that the wires should have extremely high strength, and that little plastic deformation will occur since the slip process will be limited [57]. Overall, a rather small area reduction was observed at the NW fracture surfaces, and this appears consistent with numerical modelling of 20 nm thick NW also suggests that fracture will be rather brittle when their length is over 1.5 μm [58]. Nevertheless, the NW second phase has a high strength, and is crucial for reinforcement in these bonded joints.

In comparison, the 0 % NW sample exhibited fracture surface dominated by NP with few bonded points, and so the above noted behaviours of Ag NWs were not available to dissipate the fracture energy during loading, leading to inferior strength and toughness. A schematic representation of the mechanisms occurring during fracture is illustrated in Fig. 10 which summarizes the reinforcement mechanisms provided by NWs in the bonded joints. In Fig. 10a, the inter-particle forces cause crack blunting by NP–NP

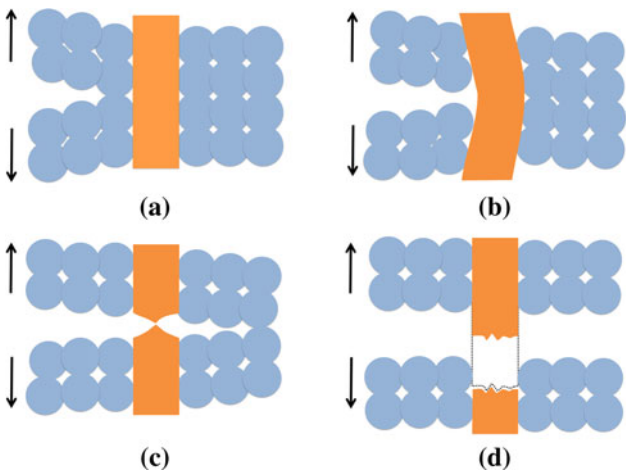

Fig. 10 Schematic mechanisms of Ag NWs reinforcement in Ag NP/NW joints: **a** Energy absorption causing crack closure by NP–NP debonding and crack propagation (NP–NP bond < stress on crack tip). **b** While the crack grows in front of Ag NW, the deformation splits along the NW and forms a compressive stress then bends the NW. The dispersed strain and energy consumption of bending NW stops the crack propagation or causes crack deflection (stress on crack tip < NW yield strength < NP–NW bond). **c** Deformation or even breaking of NW (NW-yield strength < stress on crack tip < NP–NW bond). **d** NW being pulled-out by debonding of NP–NW and further diversion of the crack (NP–NW bond < stress on crack tip). New generated smaller crack can propagate in the debonded areas

debonding and crack widening if the stress on at the crack tip is larger than the NP–NP debonding force [59, 60]. While the crack grows in the vicinity of NWs, the crack-opening stress could be released along the NW and form a local compressive stress which bends the NW as shown in Fig. 10b. The strain and energy required for bending of a NW will suppress the propagation of cracks or cause the crack deflection effectively reinforcing the joint [61, 62]. If the bonding strength of NP–NW is larger than the yield strength of NW, then deformation or even breakage of the NW could occur under loading (Fig. 10c). In the case that bonding with the NP matrix is poor around a NW, it could also be pulled-out by the debonding of NP–NW and NP–NP interfaces in Fig. 10d. After an NW has been pulled-out, a new smaller crack is easily to be generated and propagated along the debonding plane. Both crack closure and creation will dissipate the external fracture energy and thereby improve the strength of joint [63–65].

During packaging, assembly and in operation of microelectronic circuits, commercial solder joints with poor ductility may be subjected to mechanical stress and result in failure of the components [6, 66]. The damage tolerance of such microelectronic joints could be improved by replacing the solder with sintered NP/NW nanomaterial joints such as studied in this study. Such joints would dissipate the fracture energy and provide crack suppression during loading and consequently increase the reliability of the joints. It has been demonstrated that Ag NWs in these joints act as a reinforcing phase to improve the strength of bonded samples by absorbing the strain energy consumption during loading.

Conclusions

Joints with high strength and fracture energy where produced by low temperature sintering of Ag NP/NW mixed pastes in a pressureless bonding method used to join Cu wires. The addition of 20 vol% Ag NW improved the strength of joints bonded at low temperature (60–150 °C) by 50–80 %. Interfacial fracture dominated at the Cu/Ag interface at the Cu wire surface when Ag NWs were added into the paste; however, Cu and Ag were found to form a metallic bond during the low temperature pressureless sintering procedure. The addition of 20 % Ag NWs introduced provided crack deflection and fracture energy absorption during loading of the joints via mechanisms of Ag NW bending, deformation, breaking and pull-out. When the NW volume fraction was increased to 30 % the bonding paste become highly porous and the mechanical properties severely degraded. The low temperature pressureless sintering process with Ag NP/NW mixed pastes appears to be a potential alternative for conventional lead alloy solders for flexible electronics interconnections and lead-free microelectronics packaging.

Acknowledgements This study was jointly supported by the Canadian Research Chairs (CRC) program, a strategic project grant of National Sciences and Engineering Research Council (NSERC) and the State Scholarship Fund of China (No. 2010640009). The authors would like to acknowledge the comments and suggestions of Prof. Scott Lawson, Dr. Xiaogang Li and Mr. Hong Huang from the Centre for Advanced Materials Joining at the University of Waterloo.

References

1. Li Y, Moon K, Wong C (2005) Science 308:1419
2. Tu K, Gusak A, Li M (2003) J Appl Phys 93:1335
3. Suganuma K (2001) Curr Opin Solid State Mater Sci 5:55
4. Glazer J (1995) Int Mater Rev 40:65
5. Frear DR, Vianco PT (1994) Metall Mater Trans A 25A:1509
6. Coughlin JP, Williams JJ, Crawford GA, Chawla N (2009) Metall Mater Trans A 40A:176
7. Zeng K, Tu KN (2002) Mater Sci Eng R 38:55
8. Lu Y, Huang JY, Wang C, Sun S, Lou J (2010) Nat Nanotech 5:218
9. Cui Q, Gao F, Mukherjee S, Gu Z (2009) Small 5:1246
10. Hu L, Pasta M, Mantia FL, Cui L, Jeong S, Deshazer HD, Choi JW, Han SM, Cui Y (2010) Nano Lett 10:708
11. Zeng X, Zhang Q, Yu R, Lu C (2010) Adv Mater 22:4484
12. Sirringhaus H, Kawase T, Friend RH, Shimoda T, Inbasekaran M, Wu W, Woo EP (2000) Science 290:2123
13. Lee WF, Tsao KT (2010) J Mater Sci 45:89. doi:10.1007/s10853-009-3896-7
14. Ridley B, Nivi B, Jacobson JM (1999) Science 286:746
15. Redinger D, Molesa S, Yin S, Farschi R, Subramanian V (2004) IEEE Trans Electron Dev 51:1978
16. Yung KC, Wu SP, Liem H (2009) J Mater Sci 44:154. doi:10.1007/s10853-008-3119-7
17. Kim D, Moon J (2005) Electrochem Solid State Lett 8:J30
18. Lee HH, Chou KS, Huang KC (2005) Nanotechnology 16:2436
19. Zhou Y (2008) Microjoining and Nanojoining. Woodhead Publishing Ltd, CRC Press, Cambridge
20. Hu A, Guo JY, Alarifi H, Patane G, Zhou Y, Compagnini G, Xu CX (2010) Appl Phys Lett 97:153117
21. James C, Chakraborty T, Brown A, Comyn T, Dorey R, Harrington J, Laister AJ, Miles RE, Puchmark C, Xu B, Xiong W, Zhang Q, Milne SJ (2009) J Mater Sci 44:5325. doi:10.1007/s10853-009-3609-2
22. Ide E, Angata S, Hirose A, Kobayashi KF (2005) Acta Mater 53:2385
23. Bai JG, Zhang ZZ, Calata JN, Lu GQ (2006) IEEE Trans Compon Pack Technol 29:589
24. Yan J, Zou G, Hu A, Zhou Y (2011) J Mater Chem 21:15981
25. Bakhishev T, Subramanian V (2009) J Electron Mater 38:2720
26. Alarifi H, Hu A, Yavuz M, Zhou Y (2011) J Electron Mater 40:1394
27. Buffat P, Borel JP (1976) Phys Rev A 13:2287
28. Gibson RF (2010) Compos Struct 92:2793
29. Domenici V, Conradi M, Remškar M, Viršek M, Zupančič B, Mrzel A, Chambers M, Zalar B (2011) J Mater Sci 46:3639. doi:10.1007/s10853-011-5280-7
30. Espinosa HD, Juster AL, Latoure FJ, Loh OY, Gregoire D, Zavattieri PD (2011) Nat Commun 2:173
31. Bai H, Li C, Shi G (2011) Adv Mater 23:1089
32. Naslain R (2004) Compos Sci Technol 64:155

33. Guicciard S, Silvestroni L, Nygren M, Sciti D (2010) J Am Ceram Soc 98:2384
34. Lee KS, Jang KS, Park JH, Kim TW, Han IS, Woo SK (2011) Mater Des 32:4394
35. Zhang L, Yang H, Guo X, Shen J, Zhu X (2011) Scr Mater 65:186
36. Pemberton SR, Oberg EK, Dean J, Tsaroucha D, Markaki AE, Marston L, Clyne TW (2011) Compos Sci Technol 71:266
37. Yang J, Li S, Luo Y, Yan L, Wang F (2011) Carbon 49:1542
38. Coughlin JP, Williams JJ, Chawla N (2009) J Mater Sci 44:700. doi:10.1007/s10853-008-3188-7
39. Gao PX, Lao CS, Hughes WL, Wang ZL (2005) Chem Phys Lett 408:174
40. Zhang ZX, Chen XY, Xiao F (2011) J Adhes Sci Technol 25:1465
41. Yadav GG, Zhang G, Qiu B, Susoreny JA, Ruan X, Wu Y (2011) Nanoscale 3:4078
42. Li X, Gao F, Gu Z (2011) Open Surf Sci J 3:91
43. Zhao X, Fuji M, Shirai T, Watanabe H, Takahashi M, Zuo Y (2011) J Mater Sci 46:4630. doi:10.1007/s10853-011-5365-3
44. Sun Y, Gates B, Mayers B, Xia Y (2002) Nano Lett 2:165
45. Sun Y, Xia Y (2002) Adv Mater 14:833
46. Yuan X, Li C, Guan G, Xiao Y, Zhang D (2008) Polym Degrad Stabil 93:466
47. Zheng M, Gu M, Jin Y, Jin G (2000) Mat Sci Eng B 77:55
48. Epling WS, Hoflund GB, Salaita GN (1998) J Phys Chem B 102:2263
49. Tada H, Bronkema J, Bell AT (2004) Catal Lett 92:93
50. Krammer O, Sinkovics B (2010) Microelectron Reliab 50:235
51. Hirose A, Yanagawa H, Ide E, Kobayashi KF (2004) Sci Technol Adv Mat 5:267
52. Lei TG, Calata JN, Lu GQ (2010) IEEE Trans Compon Pack Technol 33:98
53. Zhao B, Kwon HJ (2011) J Adhes Sci Technol 25:557
54. de Gennes PG (1971) J Chem Phys 55:572
55. Hsueh CH (1990) Mat Sci Eng A 23:1
56. Mall S, Vozzola RP, Zawada LP (1989) J Am Ceram Soc 72:1175
57. Leach AM, McDowell M, Gall K (2007) Adv Funct Mater 17:43
58. Wu Z, Zhang YW, Jhon MH, Gao H and Srolovitz DJ (2012) Nano Lett 12(2):910. doi:10.1021/nl203980u
59. Iyengar N, Curtin WA (1997) Acta Mater 45:1489
60. Chermant JL, Boitier G, Darzens S, Farizy G, Vicens J, Sangleboeuf JC (2002) J Eur Ceram Soc 22:2443
61. Vaughan TJ, McCarthy CT (2011) Compos Sci Technol 71:388
62. Rödel J (1992) J Eur Ceram Soc 10:143
63. Suemasu H, Kondo A, Itatani K, Nozue A (2001) Compos Sci Technol 61:281
64. Suzuki T, Sato M, Sakai M (1992) J Mater Res 7:2869
65. Liao H, Wu Y, Wu M, Liu H (2011) Polym Compos 32:837
66. Terashima S, Yoshiharu K, Takuya H, Masamoto T (2003) J Electron Mater 32:1527